Yulia Grebenyuk (Autor)

Experimental and Theoretical Investigations of Wicking in Porous Media

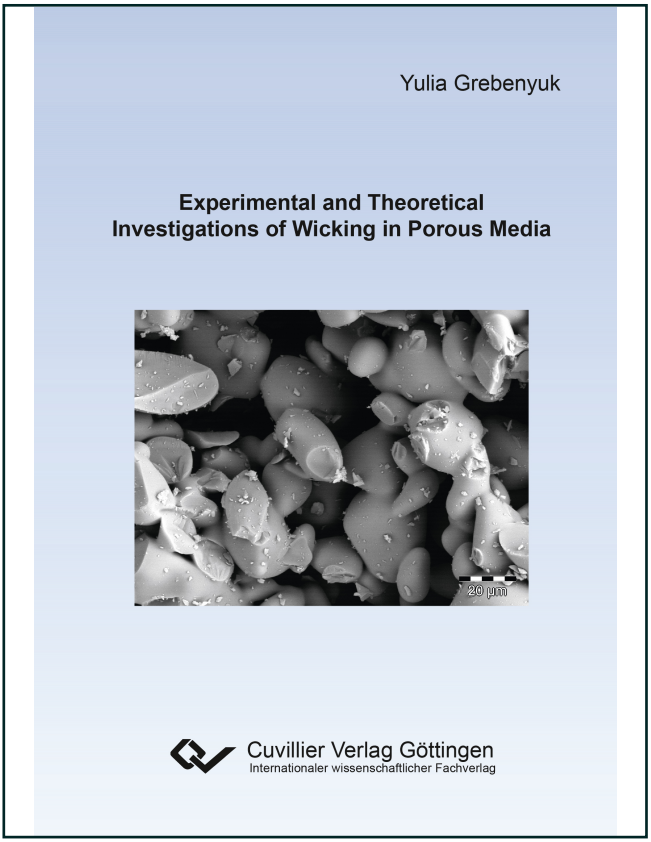

https://cuvillier.de/de/shop/publications/7737

Chapter 1

Introduction

1.1 Motivation

This section is based on the publications "Wicking of liquid nitrogen into superheated porous structure"[1] by Y. Grebenyuk and M.E. Dreyer [34] and "Wicking into porous polymer-derived ceramic monoliths fabricated by freeze-casting"[2] by Y. Grebenyuk et al. [160].

Porous materials have found a wide range of applications in a variety of industry branches. Due to the high specific surface area and the ability to conduct a fluid flow, such materials became an effective tool to implement the heat and mass transfer processes. This is of particular interest, for example, in heat pipes technologies [18, 19, 26] and catalyst support in chemical reactors [20, 21, 22]. Mass transport and structure characteristics of porous materials are essential for filtration technologies [23, 24, 25] and textile production [27, 28, 78].

Moreover, porous materials are applied in the space industry for phase separation and transport of storable and cryogenic fluids. Vapor-free propellant delivery to the engines is of importance for all space mission stages. In the absence of gravity, however, liquid-gas separation becomes challenging. For that reason, propellant management devices (PMD) can be implemented inside propellant tanks. Capillary pressure driven flow is an effective solution to enable vapor-free liquid delivery. Based on this principle, PMDs with porous screen elements [118, 119, 146] were designed. A screen PMD, or a screen channel liquid acquisition device (LAD), includes several porous elements that get saturated with a liquid and ensure the liquid transport through

[1] Reprinted from Cryogenics, Vol. 78, Y. Grebenyuk, M.E. Dreyer, Wicking of liquid nitrogen into superheated porous structures, Pages No. 27-39, Copyright (2017), with permission from Elsevier.

[2] Reprinted from Journal of the European Ceramic Society, Vol. 37, Y. Grebenyuk, H.X. Zhang, M. Wilhelm, K. Rezwan, M.E. Dreyer, Wicking into porous polymer-derived ceramic monoliths fabricated by freeze-casting, Pages No. 1993-2000, Copyright (2017), with permission from Elsevier.

them due to the capillary pressure. Vapor ingestion is blocked until the screen bubble point pressure is not exceeded. An influence of the screen parameters on the LAD performance was investigated in [120, 121, 122]. Furthermore, venting might be necessary during ballistic flight phases which could lead to liquid expulsion via the gas ports of upper stage propellant tanks. A gas phase port separator was designed to prevent this undesired effect [123]. The device includes double porous screen elements which shall avoid the expulsion of liquid propellant during venting. A double porous screen element concept and a theoretical model are given in [72].

Evaporation in porous elements can diminish the performance of liquid-vapor separation devices or even lead to their operation failure. Some studies were performed to investigate this effect for storable liquids [125, 126]. Meanwhile, cryogenic fluids are widely used in the spaceflight community for high performance propulsion systems. Liquid oxygen and hydrogen are the most common cryogenic propellants. Such liquids are characterized by low surface tension values and low normal boiling point temperature. For that reason the capillary transport of cryogenic liquids subjected to evaporation requires a thorough investigation and analysis.

The application of porous ceramics for transport of cryogenic liquids may increase technical efficiency and reduce production and maintenance costs. Properties of porous ceramics including high specific surface area, chemical and thermal stability, corrosion resistance and controllable surface characteristics can be adjusted by applying different techniques, like sacrificial templating, direct foaming or freeze casting method, which give different structures and pore size ranges [150, 25, 151]. For the spaceflight community a substantial benefit is the relatively light weight of porous ceramics compared to metallic elements used nowadays. However, porous ceramics have to fulfil the requirements of the aerospace industry concerning mechanical integrity and cleanliness. A special attention has recently been drawn to anisotropic porous materials [147, 148, 149]. The properties of these materials are directionally dependent. That allows to adjust porous structures to particular needs of certain devices and to improve their performance.

The aim of this work is to advance the knowledge on the behavior of fluids in porous materials. The wicking process was investigated. Wicking, or imbibition, is a spontaneous penetration of liquid into porous media driven by capillary forces. Due to the challenges of the capillary transport of cryogenic liquids described above, the wicking of liquid nitrogen subjected to evaporation was of a special interest for this research. For that, a novel test facility was built to perform wicking experiments in a one-species system under pre-defined non-isothermal conditions. Two one-dimensional macroscopic wicking models were proposed to evaluate the

impact of the porous sample superheat, geometrical and structural characteristics as well as the impact of the vapor flow created due to evaporation. In the second part of this work, the capillary transport abilities of porous ceramic monoliths of an anisotropic structure were investigated. The polymer-derived ceramic samples fabricated via freeze-casting method were characterized via vertical wicking tests. In the third part, the capillary transport properties of porous media and the wicking process were studied using the computational fluid dynamics software. The results of benchmark microscopic and macroscopic simulations of fluid flow problems in porous media were discussed.

1.2 Outline

This work is divided into eight chapters. The theoretical background necessary for the understanding of the investigated problems and the state of the art are given in chapter 2.
Chapter 3 describes the macroscopic approach applied in this study for modeling of the wicking process. It also presents the derivation of governing equations for the proposed one-dimensional theoretical models. The models account for evaporation occurring at the wicking front due to the heat transfer between superheated porous media and cryogenic liquid at saturation temperature. The dimensionless scaling of the model variables and parameters is shown.
Chapter 4 provides information on the experimental apparatus as well as the experiment preparation and methodology for wicking tests with liquid nitrogen (cryo-wicking) and superheated porous samples. The analysis of the experiment data and its comparison with the theoretical model predictions are discussed. The results are presented in dimensionless form.
In chapter 5 the results of wicking experiments with liquid nitrogen and sealed superheated porous samples are summarized. The sealing was applied in order to investigate the influence on the imbibition process of the vapor flow created due to the heat transfer at the wicking front. The experiment data were compared to the results for the samples with no sealing. The theoretical model prediction is given. The dimensionless form of the results is discussed.
Chapter 6 describes the findings of the investigation of the capillary transport abilities of porous polymer-derived ceramic monoliths. The monoliths revealed an anisotropic structure and were characterized using vertical wicking experiments at different sample orientation.
The study of the capillary transport properties of porous media and the wicking process performed using the computational fluid dynamics software FLOW-3D is described in chapter 7. The chapter provides information on the computation approach, relevant equations and numerical approximations applied for fluid flow simulations. The microscopic simulations were

performed for the steady fluid flow and the wicking process in porous media. The macroscopic wicking simulation was conducted. The analysis of the simulation results and their comparison with the theoretical model prediction and experiment data are shown.
Chapter 8 provides a conclusion based on the results obtained in this study.

Chapter 2

Theoretical background and state of the art

This chapter provides the theoretical background required for the understanding of the phenomena studied in this work and describes the state of the art on the characterization of porous media and the wicking process. The latter is a spontaneous penetration of liquid into porous media due to capillary forces. An overview of the theoretical approaches and experimental investigations of wicking is given. The application of computational fluid dynamics software for wicking simulations is discussed.

2.1 Surface tension

If a liquid is unable to expand freely, an interface is formed with a second fluid phase [4]. This phenomenon is due to the fact that the molecules at the interfacial surface are unbalanced and attract to each other by van der Waals forces. It results in an effect that the surface is in tension. If an element $\mathrm{d}l$ is defined on the interfacial surface between the liquid and gas, then this element is excerted to a force $\sigma \mathrm{d}l$ which is tangential to the surface. The coefficient σ is called the surface tension of the liquid. The free surface tends to minimize. Therefore, a certain amount of work $\sigma \mathrm{d}A$ is required to be done in order to increase the surface [4]. This is an alternative approach to introduce the concept of the surface tension.

Generally the surface tension of liquids decreases with an increasing pressure and temperature and is equal to zero at the critical point [4].

The most common methods to determine the surface tension of liquids are the ring method [8, 9], the maximum bubble pressure method [10, 11], the drop-weight-method [12, 13] and the Wilhelmy plate method [14, 15, 16].

2.2 Contact angle

Wicking process in porous media always involves a solid and at least two fluid phases. A drop of liquid placed on a smooth, plain solid surface in a gaseous environment is depicted on Fig. 2.1. Here three different interfaces are present: liquid-gas, solid-gas and liquid-solid. These three interfaces meet in a contact line (a contact point for two-dimensional case). Fig. 2.1 displays the directions of the interfacial forces, where σ is the surface tension of the liquid, σ_{SG} is the interfacial tension between the solid and gas (or the surface tension of the solid), and σ_{SL} is the interfacial tension between the liquid and solid. In fact, each interface is characterized by the interfacial tension. However, the determination of the interfacial tension between the solid and gas σ_{SG} and between the solid and liquid σ_{SL} is much more complicated than the determination of the surface tension for liquids σ [29, 30]. If the drop is in equilibrium, a finite angle θ is formed between the liquid-gas and solid-liquid interfaces. The angle θ is called the static contact angle. The balance of the interfacial forces parallel to the solid surface yields the Young equation [1]

$$\sigma \cos\theta = \sigma_{\mathrm{SG}} - \sigma_{\mathrm{SL}}. \tag{2.1}$$

Depending on the value of the static contact angle θ, the liquid is referred to as perfectly wetting, wetting and non-wetting. A perfectly wetting liquid has a zero static contact angle,

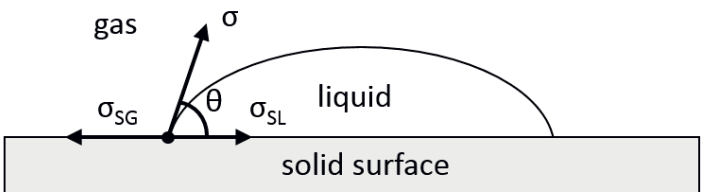

Figure 2.1: A drop of liquid placed on a smooth, plain solid surface in a gaseous environment. The directions of the interfacial tensions are shown via the arrows: σ is the surface tension of the liquid, σ_{SG} is the interfacial tension between the solid and gas (or the surface tension of the solid), and σ_{SL} is the interfacial tension between the liquid and solid. A finite angle θ formed between the liquid-gas and solid-liquid interfaces is the static contact angle.

i.e. $\theta = 0°$. For $0° < \theta < 90°$ the liquid is referred to as wetting. For $90° \leq \theta < 180°$ it is referred to as the non-wetting liquid. In this work wicking in porous media has been studied for a cryogenic liquid (nitrogen) and FC-72 liquid. Both, cryogenic liquids and the FC-72 liquid are identified as perfectly-wetting with a variety of materials [31, 32, 33, 34, 36, 126, 38, 39, 40]. On the actual geometry of a rough solid surface the contact angle may significantly differ from the one given by the Young equation. A relation between the Young static contact angle θ and the apparent contact angle θ^*_{w} observed on the rough surface can be expressed by the Wenzel's equation [35]

$$\cos\theta^*_{\mathrm{w}} = r\cos\theta, \tag{2.2}$$

where $r = A/A_0$ is the roughness of the surface given as a ratio of the real surface area A to the projected surface area A_0. In this model it is assumed that the liquid conforms the solid topography. However, in case of very rough and hydrophobic surfaces a gas can be trapped in the interstices on the solid surface [35]. This effect is implemented in the Cassie model that defines a relation between the Young static contact angle θ and the apparent contact angle θ^*_{c} as [35]

$$\cos\theta^*_{\mathrm{c}} = (1 - \phi_{\mathrm{g}})\cos\theta - \phi_{\mathrm{g}}, \tag{2.3}$$

where ϕ_{g} is the area fraction of the surface filled with the gas. The effect of the rough surfaces is not considered in this work.

If the contact line moves, the contact angle changes and is referred to as the dynamic contact angle θ_{d}. For the advancing and receding contact lines one should also distinguish between the advancing and receding contact angles [1, 35, 16]. The dynamic contact angle θ_{d} changes with the contact line velocity u parallel to the solid surface. Therefore, it can be connected to the capillary number given as

$$\mathrm{Ca} = \frac{\mu_{\mathrm{L}} u}{\sigma}, \tag{2.4}$$

where μ_{L} is the dynamic viscosity of the liquid. Some empirical correlations were proposed to state a relation between the capillary number, the dynamic and static contact angles [41, 42, 43]. For the advancing contact line formed with a perfectly-wetting liquid and for $\mathrm{Ca} < 0.1$ the dynamic contact angle can be calculated as [44, 45]

$$\theta_{\mathrm{d}} = 4.54\ \mathrm{Ca}^{0.353}. \tag{2.5}$$

In this study the wicking phenomena occurred at small capillary numbers ($\mathrm{Ca} < 2 \cdot 10^{-4}$, see sections 4.4.5 and 5.4.4). The calculation of the dynamic contact angle for such capillary numbers via Eq. 2.5 gives some insignificant deviations from zero. Therefore, in this work the contact angle was taken as $\theta_{\mathrm{d}} = \theta = 0°$.

2.3 Young-Laplace equation

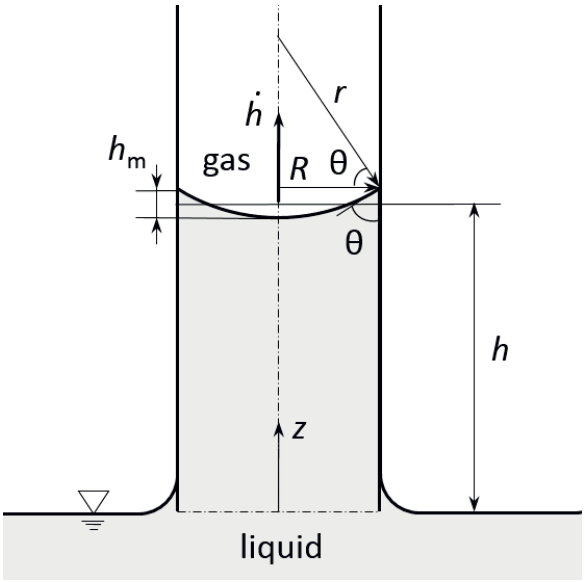

Figure 2.2: The liquid rise in the capillary of an internal radius R. The spherical meniscus of a principal radius of curvature $r = R/\cos\theta$ is formed between the liquid, the gaseous phase and the solid walls of the capillary. h_{m} is the height of the meniscus. The angle formed between the walls of the capillary and the liquid-gas interface is the contact angle θ. h is the liquid height that relates the total volume of liquid in the tube and the volume of a liquid column with a flat surface. $\dot{h}$ is the meniscus velocity.

In case of a curved free interface, there is a pressure difference between the liquid and the second fluid phase. The pressure is higher on a concave side of the interface. For an arbitrary interface with principal radii of curvature r_1 and r_2, this pressure difference $\triangle p$ is given by the Young-Laplace equation [1]

$$\triangle p = \sigma \left(\frac{1}{r_1} + \frac{1}{r_2} \right), \tag{2.6}$$

where for the liquid-gas interface σ is the surface tension of the liquid. The derivation of the Young-Laplace equation is shown, for example, by Dullien [1].

Wicking into a pore is often implied to be analogous to the liquid rise in a small circular capillary. Fig. 1 displays a liquid rise in the capillary of an internal radius R. An interface formed between the liquid, the gaseous phase and the solid walls of the capillary is called the meniscus. The angle formed between the walls of the capillary and the liquid-gas interface is the contact angle θ, see Fig. 1. The Bond number Bo characterizes the ratio of the gravitational force to the surface tension and given as

$$\mathrm{Bo} = \frac{\rho_{\mathrm{L}} g R^2}{\sigma}, \tag{2.7}$$

where ρ_{L} is the density of liquid and g is the gravitational acceleration. In case of a small capillary, Bo $<<$ 1 and the meniscus of a spherical shape can be assumed. Therefore, the principal radii of curvature for the interface are $r_1 = r_2 = R/\cos\theta$. Thus, applying the Young-Laplace equation for a circular capillary, one obtains

$$\triangle p = \frac{2\sigma\cos\theta}{R}, \tag{2.8}$$

where the pressure difference $\triangle p$ is also called the capillary pressure.
The height of a spherical meniscus can be calculated as [46]

$$h_{\mathrm{m}} = R\left(\frac{1}{\cos\theta} - \tan\theta\right). \tag{2.9}$$

2.4 Conservation equations

2.4.1 Control volume

To describe fluid motion the basic equations of mass, linear momentum and energy conservation can be written for an infinitesimally small control volume. A control volume of a infinitesimal size dx, dy and dz in x-,y- and z-directions, respectively, was defined in the Cartesian coordinates (x, y, z). Such an approach provides differential equations of fluid motion.

2.4.2 Mass conservation

The mass conservation equation for an infinitesimal control volume defined in the Cartesian coordinates (x, y, z) yields [4]

$$\frac{\partial\rho}{\partial t} + \frac{\partial}{\partial x}(\rho u) + \frac{\partial}{\partial y}(\rho v) + \frac{\partial}{\partial z}(\rho w) = 0, \tag{2.10}$$

where t is time, ρ is the density of fluid, u, v and w are the velocity components in x-,y- and z-directions, respectively.
For the incompressible fluid Eq. 2.10 reduces to

$$\frac{\partial u}{\partial x} + \frac{\partial v}{\partial y} + \frac{\partial w}{\partial z} = 0. \tag{2.11}$$

Using the Nabla operator ∇ given with unit vectors $\mathbf{i}$, $\mathbf{j}$, and $\mathbf{k}$ as

$$\nabla = \mathbf{i}\frac{\partial}{\partial x} + \mathbf{j}\frac{\partial}{\partial y} + \mathbf{k}\frac{\partial}{\partial z}, \tag{2.12}$$

Eqs. 2.10 and 2.11 can be written in a compact form as

$$\frac{\partial \rho}{\partial t} + \nabla \cdot (\rho \boldsymbol{v}) = 0, \tag{2.13}$$

$$\nabla \cdot \boldsymbol{v} = 0, \tag{2.14}$$

respectively. The vector $\boldsymbol{v}$ in Eqs. 2.13 and 2.14 is the velocity vector given as

$$\boldsymbol{v} = \mathbf{i}u(x,y,z,t) + \mathbf{j}v(x,y,z,t) + \mathbf{k}w(x,y,z,t). \tag{2.15}$$

2.4.3 Linear momentum conservation

The momentum conservation equations for an infinitesimal control volume defined in the Cartesian coordinates (x, y, z) yield [4]

$$\rho\left(\frac{\partial u}{\partial t} + u\frac{\partial u}{\partial x} + v\frac{\partial u}{\partial y} + w\frac{\partial u}{\partial z}\right) = -\frac{\partial p}{\partial x} + \frac{\partial \tau_{xx}}{\partial x} + \frac{\partial \tau_{yx}}{\partial y} + \frac{\partial \tau_{zx}}{\partial z} + \rho G_x, \tag{2.16}$$

$$\rho\left(\frac{\partial v}{\partial t} + u\frac{\partial v}{\partial x} + v\frac{\partial v}{\partial y} + w\frac{\partial v}{\partial z}\right) = -\frac{\partial p}{\partial y} + \frac{\partial \tau_{xy}}{\partial x} + \frac{\partial \tau_{yy}}{\partial y} + \frac{\partial \tau_{zy}}{\partial z} + \rho G_y, \tag{2.17}$$

$$\rho\left(\frac{\partial w}{\partial t} + u\frac{\partial w}{\partial x} + v\frac{\partial w}{\partial y} + w\frac{\partial w}{\partial z}\right) = -\frac{\partial p}{\partial z} + \frac{\partial \tau_{xz}}{\partial x} + \frac{\partial \tau_{yz}}{\partial y} + \frac{\partial \tau_{zz}}{\partial z} + \rho G_z, \tag{2.18}$$

where μ is the dynamic viscosity of fluid, G_x, G_y and G_z are the body accelerations in x-,y- and z-directions, respectively. The components τ_{xx}, τ_{yy}, τ_{zz}, τ_{xy}, τ_{xz}, τ_{yz} τ_{zx}, τ_{yx} and τ_{zy} in Eqs. 2.16, 2.17 and 2.18 are the shear stresses given for Newtonian fluid as

$$\tau_{xx} = 2\mu\frac{\partial u}{\partial x} - \frac{2}{3}\mu\left(\frac{\partial u}{\partial x} + \frac{\partial v}{\partial y} + \frac{\partial w}{\partial z}\right), \tag{2.19}$$

$$\tau_{yy} = 2\mu\frac{\partial v}{\partial y} - \frac{2}{3}\mu\left(\frac{\partial u}{\partial x} + \frac{\partial v}{\partial y} + \frac{\partial w}{\partial z}\right), \tag{2.20}$$

$$\tau_{zz} = 2\mu\frac{\partial w}{\partial z} - \frac{2}{3}\mu\left(\frac{\partial u}{\partial x} + \frac{\partial v}{\partial y} + \frac{\partial w}{\partial z}\right), \tag{2.21}$$

$$\tau_{xy} = \tau_{yx} = \mu\left(\frac{\partial v}{\partial x} + \frac{\partial u}{\partial y}\right), \tag{2.22}$$

$$\tau_{xz} = \tau_{zx} = \mu\left(\frac{\partial u}{\partial z} + \frac{\partial w}{\partial x}\right), \tag{2.23}$$

$$\tau_{yz} = \tau_{zy} = \mu\left(\frac{\partial v}{\partial z} + \frac{\partial w}{\partial y}\right). \tag{2.24}$$

For an incompressible fluid the components τ_{xx}, τ_{yy} and τ_{zz} (see Eqs. 2.19, 2.20 and 2.21) transform to

$$\tau_{xx} = 2\mu\frac{\partial u}{\partial x}, \tag{2.25}$$